

Vibrational Spectroscopy of Aqueous Sodium Halide Solutions and Air–Liquid Interfaces: Observation of Increased Interfacial Depth

Dingfang Liu, Gang Ma, Lori M. Levering, and Heather C. Allen*

Department of Chemistry, The Ohio State University, 100 West 18th Avenue, Columbus, Ohio 43210

Received: March 27, 2003; In Final Form: December 9, 2003

Air–aqueous sodium halide solution interfaces are examined using vibrational sum frequency generation spectroscopy. Raman and ATR-FTIR (attenuated total reflection Fourier transform infrared) spectroscopies are also used to compare the effects of halide anions on the water structure of the bulk solution to that of the interface. The interfacial water structures for the sodium fluoride and chloride aqueous solutions are found to be similar to the air–water interface, whereas sodium bromide and iodide aqueous solutions cause significant distortion of the hydrogen-bonding network. Analysis of the spectra indicates higher concentrations of bromide and iodide anions in the interfacial region with an increase in interfacial depth.

Introduction

The frequent and sudden decrease of ozone concentration in the lower troposphere of the Arctic at polar sunrise has been observed for over a decade.^{1–3} Catalytic reactions involving reactive halogen atoms are considered to be the major contributing factor to the Arctic tropospheric ozone depletion.^{4–6} The oxidation of halide anions in sea salt aerosol, snow, and the frozen ocean surface^{7–10} has been shown to yield active halogen compounds such as BrO.^{11,12} These oxidation processes occur not only in the bulk liquid but also at air–liquid interfaces, and the latter may play a crucial role in the uptake and reaction of gases with droplets in the troposphere.⁵ Reactions between gases (e.g., O₃) and halide anions are enhanced at the interface compared to the bulk solution.¹³ Aerosol chamber experiments, molecular dynamics (MD), and kinetic modeling studies found that measurements of the gaseous molecular chlorine products are explainable only if reactions at the air–water interface are dominant.⁵

Although the existence of halide ions in the interfacial region has been postulated from recent studies,^{5,13} direct experimental measurement of this phenomenon has remained elusive due to the difficulties inherent in measuring the structure and composition of air–liquid interfaces. In terms of the Gibbs adsorption equation, interpretation of the traditional theory suggests that there are no atomic ions at the air–solution interface.^{14–16} On the contrary, recent molecular dynamics simulations by Jungwirth and Tobias^{16,17} reveal that although the small, nonpolarizable fluoride anion is excluded from the air–water interface, the larger more polarizable halide anions are present in the interfacial region. Bromide and iodide anions are shown to have higher concentrations in the interfacial region than in the bulk.^{16,17} This theoretical picture of ions at the air–liquid interface can be tested by interface-selective spectroscopic techniques. In this study, vibrational sum frequency generation (SFG) spectroscopy, an interface-selective spectroscopy, is used to investigate the interfacial water structure of several aqueous sodium halide air–solution interfaces.

The theory of SFG has been described previously.^{18–22} However, a brief overview of SFG theory is presented here since

it is the focus of this work. SFG is a second-order nonlinear process that occurs in noncentrosymmetric environments such as interfaces under the electric dipole approximation. The SFG intensity, I_{SFG} , as shown in eq 1,

$$I_{\text{SFG}} \propto |\chi^{(2)}|^2 = |\chi_{\text{NR}}^{(2)} + \sum_v \chi_v^{(2)}|^2 \quad (1)$$

is proportional to the absolute square of the macroscopic second-order nonlinear susceptibility, $\chi^{(2)}$, which consists of resonant terms ($\chi_v^{(2)}$) and a nonresonant term ($\chi_{\text{NR}}^{(2)}$). When the frequency of an incident infrared beam, ω_{IR} , is resonant with a vibrational mode of an interfacial molecule, v , the resonant susceptibility term $\chi_v^{(2)}$ dominates $\chi^{(2)}$ and a SFG intensity enhancement is observed. $\chi_v^{(2)}$ is shown in eq 2,

$$\chi_v^{(2)} \propto \frac{A_v}{\omega_v - \omega_{\text{IR}} - i\Gamma_v} \quad (2)$$

where A_v is the amplitude of the transition moment, v is the frequency of the transition moment, and Γ_v describes the line-width of the transition. The amplitude, A_v , is nonzero when the Raman and the infrared transitions are spectroscopically allowed. The macroscopic nonlinear susceptibility $\chi^{(2)}$ is related to the molecular susceptibility, $\beta_{lmn,v}$. The molecular susceptibility can be described by eq 3,

$$\beta_{lmn,v} = \frac{\langle g|\alpha_{lm}|v\rangle\langle v|\mu_n|g\rangle}{\omega_{\text{IR}} - \omega_v + i\Gamma_v} \quad (3)$$

where $\langle g|\alpha_{lm}|v\rangle$ represents the Raman transition moment, $\langle v|\mu_n|g\rangle$ represents the IR transition moment for the molecule, and lmn represents the molecular coordination system. An Euler angle transformation relates the molecular coordinate system (l,m,n) to the laboratory coordinate system (I,J,K). The transformation is shown in eq 4

$$\beta_{IJK,v} = \sum_{lmn} \mu_{IJK:lmn} \beta_{lmn,v} \quad (4)$$

where $\mu_{IJK:lmn}$ is the Euler angle transformation between the laboratory coordinates (I,J,K) and the molecule coordinates

* Author to whom correspondence should be addressed. E-mail: allen@chemistry.ohio-state.edu.

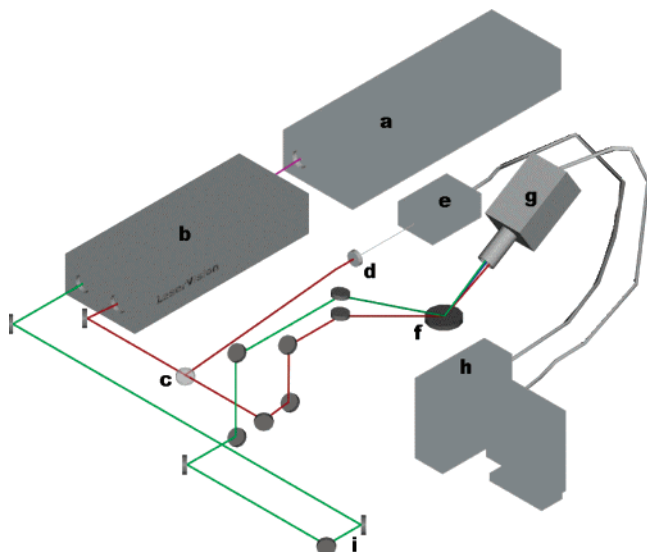


Figure 1. Schematic layout of the vibrational sum frequency generation scanning system: (a) Nd:YAG laser; (b) LaserVision OPA/OPG; (c) infrared window; (d) infrared detector; (e) energy meter; (f) sample stage; (g) CCD; (h) control computer; (i) delay line. Green, red, blue, and pink solid lines represent 532 nm, infrared, sum frequency, and 1064 nm, respectively.

(l, m, n). The macroscopic susceptibility, $\chi_{IJK,v}^{(2)}$, is therefore calculated from the molecular susceptibility, $\beta_{IJK,v}$, as shown in eq 5,

$$\chi_{IJK,v}^{(2)} = N\langle\beta_{IJK,v}\rangle \quad (5)$$

where $\chi_{IJK,v}$ is equal to the number density, N , multiplied by the orientation average of $\beta_{IJK,v}$.

The SFG spectrum, which describes the SFG intensity (I_{SFG}) as a function of the incident infrared frequency (ν), can be mathematically fit according to eq 1. When performing the mathematical fit, a constant complex number is used as the nonresonant term ($\chi_{\text{NR}}^{(2)}$) and the sign of the amplitude (A_ν) is used to denote the phase of the photons of the vibrational mode from the interfacial molecules, which incorporates orientation and relative vibrational phases. Equation 2 indicates the Lorentzian line shape in the SFG spectrum fitting. The commercially available software IGOR (version 4.0.5.1) was used in the fitting procedure after adding additional codes to describe the coherent nature of the SFG process as shown in eq 1. In Raman and IR fitting, the intensity is the summation of each vibration's intensity, whereas in SFG the intensity is the absolute square of the summation of each vibration's $\chi_\nu^{(2)}$ and $\chi_{\text{NR}}^{(2)}$ as shown in eq 1. This leads to different spectral characteristics for SFG spectra relative to Raman and IR spectra. Therefore, SFG spectra interpretation must occur after deconvolution into the component peaks because direct comparison of SFG spectra to Raman and IR spectra may be misleading, in particular for the broad bands of the hydrogen-bonding region (3000–3600 cm^{-1}).

Experimental Section

SFG Scanning System and Experimental Details. A schematic layout of the vibrational SFG scanning system is shown in Figure 1. In the Allen lab two different SFG experimental systems are available: a broad bandwidth femtosecond–picosecond SFG system^{23–28} and the SFG scanning system described here. The SFG scanning instrument was utilized for these studies because it is better suited for acquiring data of larger SFG spectral regions, in particular, the large

spectral bands of interfacial water in addition to the free OH region. The SFG experiments were carried out using a visible beam at 532 nm and an infrared beam currently tunable from 2500 to 4000 cm^{-1} with a bandwidth of $\sim 8 \text{ cm}^{-1}$ generated from a KTP-KTA based optical parametric generator/amplifier (OPG/OPA) system (LaserVision). The 532 nm beam is generated by doubling the frequency (second harmonic) of the 1064 nm pump source from an EKSPLA PL 2143 A/SS Nd:YAG laser (29 ps pulse duration and 10 Hz repetition rate).

The input 532 nm intensity is focused using a plano convex lens (CVI Laser, 500 mm focal length) and is placed $\sim 490 \text{ mm}$ before the sample surface. This provides a $\sim 1 \text{ mm}$ beam diameter and $\sim 600 \text{ mJ}$ of 532 nm light on the sample surface. The infrared beam is focused at the sample surface using a BaF_2 lens (200 mm focal length), where it has a $< 0.5 \text{ mm}$ beam diameter and $\sim 400 \mu\text{J}$. The real-time IR profiles during the SFG spectrum acquisition are also acquired. As shown in Figure 1, a BaF_2 window reflects $\sim 5\%$ (15 to 30 μJ) of the IR energy and the infrared intensity is measured by an IR probe (J9LP, Moletron Inc.) with an EPM2000 energy meter (Moletron Inc.).

The input angles are $\sim 48^\circ$ and $\sim 57^\circ$ from the surface normal for the 532 nm and infrared beams, respectively. The detection angle is set to 50.9° from the surface normal for sum frequency detection. An iris is used after the sample stage to block the main 532 nm reflection from the sample surface but allow the SFG photons to pass. A color glass filter (BG25, 2 mm thickness, CVI Laser) followed by a short pass filter (SPF500, CVI Laser) and two holographic notch plus filters (Kaiser Optical System, Inc.) in the detection system are used for filtering out the scattered 532 nm light. A 512×512 pixel array, $12.3 \text{ mm} \times 12.3 \text{ mm}$ active area, $24 \mu\text{m}$ square pixel size, back-illuminated charge-coupled device (CCD) (DV412, Andor Technology) is used to detect the sum frequency signal. The CCD is thermoelectrically (TE) cooled, and the CCD temperature was set at -45°C during the experiments. A PCI interface control card with a 16 bit A/D converter (62 kHz A/Ds for readout speeds of 62 kHz and 31 kHz) is used to control the CCD and TE cooling. In the sum frequency wavelength region the CCD provides 78% to 85% quantum efficiency. For the air–water interface in the free OH region ($\sim 3700 \text{ cm}^{-1}$), the CCD readout can reach 1000 counts (1 count = 2.5 electrons) with exposure times of 30 s and 31 kHz readout speed.

Scanning SFG system control software was programmed in our laboratory using Labview and C+ programming languages. Our program integrates automation control of the OPG/OPA servomotors, infrared energy meter (EPM2000, Moletron Inc.) control, and CCD image acquisition and data analysis. A submodule of a computational algorithm for CCD image analysis was also programmed and integrated into this SFG spectrum acquisition software in order to automatically find and track the movement of the SFG signal on the CCD array.

All of the spectra presented in this paper were acquired using a 30 s exposure time for each data point. Spectra were acquired in $\sim 40 \text{ min}$ (from 2800 to 3900 cm^{-1}). Spectra were replicated many times over a period of 15 months with 2 different pump lasers (previously a Continuum PY61). The spectra presented here are the average of two replicate spectra. At least one air–neat water spectrum was acquired at the beginning and end of the experiment to ensure the stability of the SFG system and to confirm reproducibility. A real-time background subtraction algorithm was applied, and the spectra showed that the background baseline intensity did not add to the overall intensity of the SFG spectra.

The SFG is initially optimized spatially and temporally at 3400 cm^{-1} since this is in the center of the scanning region ($2900\text{--}3900\text{ cm}^{-1}$), although significant changes are not observed with optimization in other regions of the scanning region. The SFG spectra are normalized by the SFG from a GaAs crystal since this takes into account the temporal and spatial overlap anomalies. The polarization combination used for the SFG experiments presented here are S, S, and P for the SFG, 532 nm, and infrared beams, respectively. S polarization is perpendicular to the incident plane, whereas P polarization is parallel to the incident plane. All SFG spectra were acquired at $\sim 24\text{ }^{\circ}\text{C}$.

Raman Spectroscopy. The Raman experimental setup consists of a 532 nm continuous wave (CW) laser (Spectra-Physics, Millennia II), a 5 mm focusing Raman Probe (InPhotonics, RP 532-05-15-FC), a 500 mm monochromator (Acton Research, SpectraPro SP-500) using a 600 g/mm grating, and a back-illuminated CCD (Roper Scientific, LN400EB, 1340×400 pixel array and deep depletion). Raman spectra were collected using the collection fiber optic that is part of the Raman probe, which was coupled to the entrance slit of the monochromator through an imaging fiber coupler (Acton Research, FC-446-030). SpectraSense software (Acton Research, version 4.1.9) was used for data collection and display. The power of the 532 nm beam for sample illumination was 77 mW. Before data collection, the Raman system was calibrated by using the 435.83 nm line of a fluorescence lamp and was verified by comparison to the Raman spectrum of naphthalene. Raman spectra were obtained using unpolarized light. The Raman spectral resolution and acquisition temperature were 0.8 cm^{-1} and $\sim 24\text{ }^{\circ}\text{C}$.

ATR-FTIR Spectroscopy. A Thermo Nicolet FTIR spectrometer (Avatar 370, Thermo Electron Corporation) was employed in the ATR-FTIR (attenuated total reflection Fourier transform infrared) spectroscopy experiments. The ATR measurements were made with a silicon crystal using a 45° single bounce ATR accessory (Smart SpeculATR, Thermo Electron Corporation). Spectra were collected with a spectral resolution of 4 cm^{-1} and 128 scans at a temperature of $\sim 24\text{ }^{\circ}\text{C}$.

Chemicals. Water was obtained from a Millipore Nanopure system ($18.3\text{ M}\Omega\cdot\text{m}$). Sodium halide salts (certified ACS grade) were purchased from Fisher Scientific. All of the salt solutions were checked for organic contamination by obtaining the SFG spectra of the solutions in the 2700 cm^{-1} to 3000 cm^{-1} region. The NaCl, NaBr, and NaI salts contained a significant amount of organic contamination, and therefore, an activated carbon filter (Whatman, CARBON-CAP 150) was used to remove these contaminants. The concentrations of these solutions were then verified using Raman spectroscopy by comparisons of the hydrogen-bonding region (2900 cm^{-1} to 3900 cm^{-1}). Recrystallization was sufficient to remove contaminants from the NaF salts prior to use.

Results and Discussion

The SFG spectrum, SSP polarizations, of the air–neat water interface, the Raman spectrum, and the ATR-FTIR spectrum of neat water in the OH stretch region ($2900\text{--}3900\text{ cm}^{-1}$) are shown in Figure 2 parts a–c, respectively, along with their calculated fits including the component peaks. There are several published SFG spectra of the neat air–water interface.^{29–33} The spectral features observed in our neat water surface SFG spectra are similar to previously published neat water SFG spectra.^{29–33}

The broad peaks in the $3000\text{--}3600\text{ cm}^{-1}$ region contain two prominent bands in the SFG, the Raman, and IR spectra positioned at ~ 3250 and $\sim 3450\text{ cm}^{-1}$. Following generally

accepted assignments for bulk^{34–37} and surface water,^{29,30,38} the 3250 cm^{-1} peak in the SFG (3230 cm^{-1}), the Raman (3257 cm^{-1}), and IR (3250 cm^{-1}) spectra is attributed to the strong intermolecular coupling of water molecule symmetric stretch vibrations within a symmetric hydrogen-bonding network.^{29,31} However, in the SFG spectrum this peak also includes the 3-coordinate water molecules at the surface that are single proton donor–double proton acceptor (DAA) molecules.^{39–41} The peak at $\sim 3450\text{ cm}^{-1}$ in the SFG (3446 cm^{-1}), Raman (3468 cm^{-1}), and IR (3396 cm^{-1}) spectra is assigned to the weaker coupling of the water molecule stretching modes, which is associated with a more disordered and asymmetric 4-coordinate (tetrahedral) hydrogen-bonding network.^{29,31,32,36,42–47} This peak dominates the SFG spectrum as revealed through deconvolution of the spectrum into the component peaks as shown in Figure 2a, which is consistent with recent water cluster IR studies.⁴⁰ The component peak at $\sim 3550\text{ cm}^{-1}$ (SFG at 3533 cm^{-1} , Raman at 3624 cm^{-1} , and IR at 3514 cm^{-1}) in Figure 2 parts a–c is attributed to the coupling of the OH asymmetric stretch vibrational modes,^{29,31,32} which contributes minimally to the spectra^{48,49} However, in the SFG spectra this peak also includes 3-coordinate water molecules that are double proton donor–single proton acceptor (DDA) molecules.^{39–41,50,51} The narrow peak at 3700 cm^{-1} in the SFG spectra of Figure 2a is assigned to the dangling OH (free OH) stretch of water molecules that straddle the interface with one uncoupled OH bond directed into the air phase^{29,31,32} and the other interacting through hydrogen bonding with the liquid phase as described above within the $\sim 3250\text{ cm}^{-1}$ peak assignment.^{39–41} SFG intensity is also observed on the high-frequency side of the free OH (peak at 3752 cm^{-1}). In aqueous ammonia SFG spectra Shultz et al.³⁰ found that the free OH consists of two components: a narrow resonance at 3700 cm^{-1} and a broad peak which extends $\sim 100\text{ cm}^{-1}$ beginning at 3680 cm^{-1} . Yet, the origin of this intensity is not well understood, although there is evidence supporting the assignment to the dangling OH from doubly coordinated water molecules.^{44,52} The dangling OH stretching modes from 3- and 2-coordinate water molecules were observed from amorphous ice surfaces at low temperatures using IR spectroscopy.^{44,52} Therefore, a component peak on the high-frequency side of the free OH is used to fit the SFG spectra since a nonresonant component did not compensate for the resonant-like feature particularly in the 0.036x ($x = \text{mole fraction}$) NaBr and NaI SFG spectra. (Using only a nonresonant term and allowing this to vary produces spectral fits that are slightly low on the high-frequency side of the SFG neat water spectrum as well.) SFG spectra of D_2O and NaI in D_2O in the 3000 cm^{-1} to 3900 cm^{-1} region confirmed the lack of resonant or nonresonant enhancement and are shown in Figure 4d.

To understand the hydrogen-bonding environment of water after addition of small amounts of sodium halide salts, a series of Raman and ATR-FTIR spectra were obtained for 0.015x NaF and 0.015x and 0.036x NaCl, NaBr, and NaI aqueous solutions. In Figure 3a,b, Raman spectra of these solutions are shown, and in Figure 3c,d the ATR-FTIR spectra of these same solutions are shown. The Raman spectra clearly reveal an increase in the 3450 cm^{-1} peak and a small decrease in the 3250 cm^{-1} peak. The IR spectra show a decrease in the 3250 cm^{-1} peak with narrowing of this band with increasing size of the anion added and no enhancement of the 3450 cm^{-1} peak. In both the Raman and the IR spectra, the observed trends are amplified when going from the 0.015x solution spectra to the more concentrated 0.036x

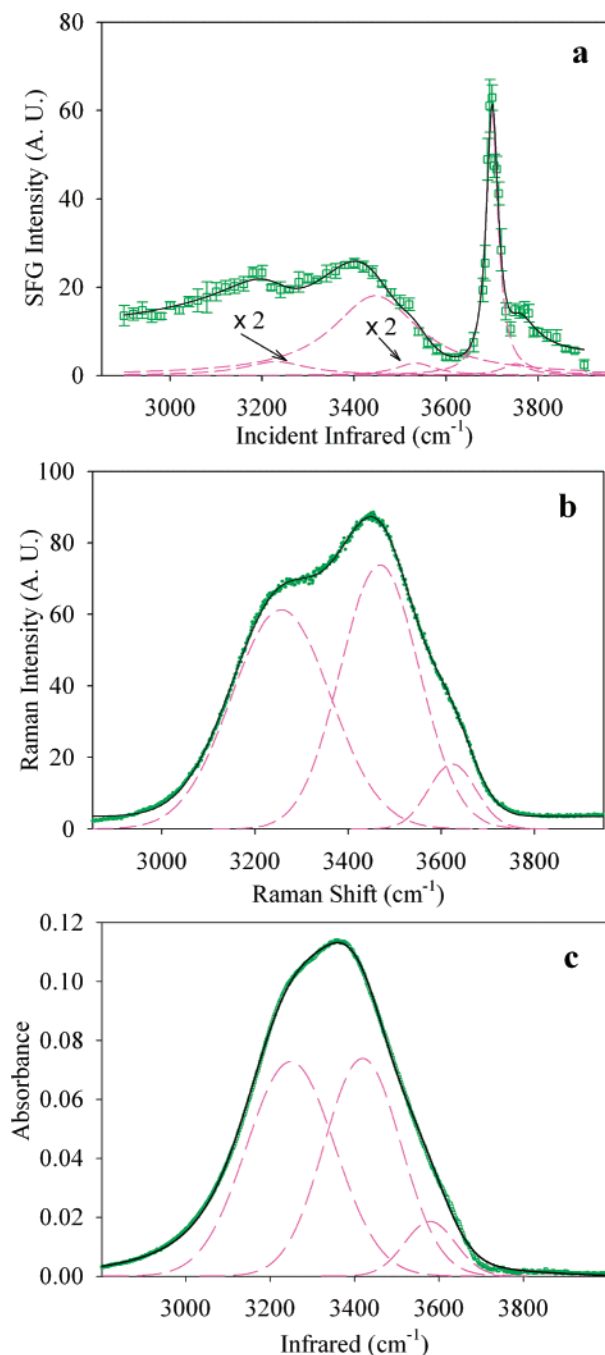


Figure 2. (a) SSP polarized SFG spectrum of neat water plotted with the fit and Lorentzian component peaks. The two SFG component peaks shown were multiplied by 2 for clarity. (b) Raman spectrum of neat water plotted with the fit and Gaussian component peaks. (c) ATR-FTIR spectrum of neat water plotted with the fit and Gaussian component peaks. For (a–c) black lines are the spectrum fits and pink dashed lines are the component peak fits.

solution spectra as well as increasing the size and polarizability of the anion added. The spectral fitting parameters are shown in Table 1.

The Raman intensity increase in the 3450 cm^{-1} region is concomitant with an increase in the polarizability of the anion in solution as stated above, where the NaI aqueous solution spectra are most affected. The water molecules are separately solvating the cation and anion. We can understand the difference in the Raman and IR spectra from the perspective of the origin of Raman and IR intensities. Raman intensity arises from polarizability changes of the transition, whereas IR intensity

originates from a change in dipole moment. The Raman and IR spectra reveal the decrease in the 3250 cm^{-1} band, and most of the intensity loss can be correlated to the displacement of the water molecules in the symmetric hydrogen-bonding network by sodium cation and the halide (iodide being the largest) ions. However, in the Raman spectrum the enhancement of the 3450 cm^{-1} peak dominates, and this is not observed in the IR spectra. With addition of salts with anions of increasing polarizability ($\text{I}^- > \text{Br}^- > \text{Cl}^- > \text{F}^-$), the water molecules that solvate these anions exhibit an increased polarizability. Thereby the solvation sphere water molecules, which are observed in the asymmetric hydrogen-bonding network, exhibit this polarizability change in the Raman spectra since Raman intensities arise from this phenomenon. And as one might expect, the fluoride anion, which is minimally polarizable, has no effect on the 3450 cm^{-1} peak in the Raman spectrum of Figure 3a. These results are consistent with previously published Raman⁵³ and IR³⁵ spectra.

The SFG spectra, SSP polarizations, for the same solutions are shown in Figure 4a–d. The surface vibrational SFG spectra from the 0.015x NaF, 0.015x NaCl, and 0.036x NaCl aqueous solutions are similar to the SFG spectrum of neat water as shown in Figure 4 parts a and b. Both data sets nearly overlap the neat water SFG spectrum. This indicates that the hydrogen-bonding environments of the air–aqueous interface of 0.015x NaF, 0.015x NaCl, and 0.036x NaCl aqueous solutions are not affected significantly. The component peaks (dashed pink lines) with the calculated fits (black solid lines going through most of the data points) are shown in the insets of Figure 4 parts a and b with the fitting parameters including relative phases (+ versus –) of the amplitude terms shown in Table 2.

Molecular dynamics simulations revealed that in the NaF solutions both ions are strongly repelled from the surface, leaving an ion-free surface layer roughly 3.5 \AA thick.^{16,17} One would not necessarily expect to observe an enhanced SFG intensity from the surface water molecules. Alignment of the water molecule's protons toward the subsurface F^- layer would not occur beyond solvation of the individual ions since the Na^+ ions are proposed to have similar concentrations to the F^- anions within the subsurface layer.¹⁶ And in fact SFG intensity changes are not observed in this study of the 0.015x NaF aqueous solution relative to that of the neat water. Yet, at this concentration, less than 0.02 water–fluoride bonds exist in the interfacial region.¹⁶ An examination of more highly concentrated solutions would be advantageous, yet the low solubility of NaF in water makes this task prohibitive in the temperature range studied here.

For NaCl aqueous solution surfaces, chloride anions are thought to occupy a portion of the air–water interface.^{16,17} Yet no significant effect on the hydrogen-bonding network from the NaCl salts was observed as shown in Figure 4b for 0.015x and 0.036x NaCl aqueous solution surfaces. A reasonable explanation is that the chloride anion polarizability is reduced in the water environment at the air–water interface.⁵⁴ This suggests that even with chloride anion present within the interfacial region, the perturbing effects on the intermolecular OH stretching bands may be insignificant at these concentrations. Previous SFG studies by Shultz et al. of NaCl aqueous solutions have also shown that chloride anions in 0.01x and 0.1x NaCl aqueous solutions had no detectable effect on the water molecules at the interface.⁵⁵ It is important to note that lack of SFG evidence for hydrogen-bonding perturbation in no way suggests lack of ion concentrations in the interfacial region. (The interface itself is defined by the gradient of concentrations of the different species, whereas the bulk begins where the concentrations are homogeneously mixed such that there is a macroscopically

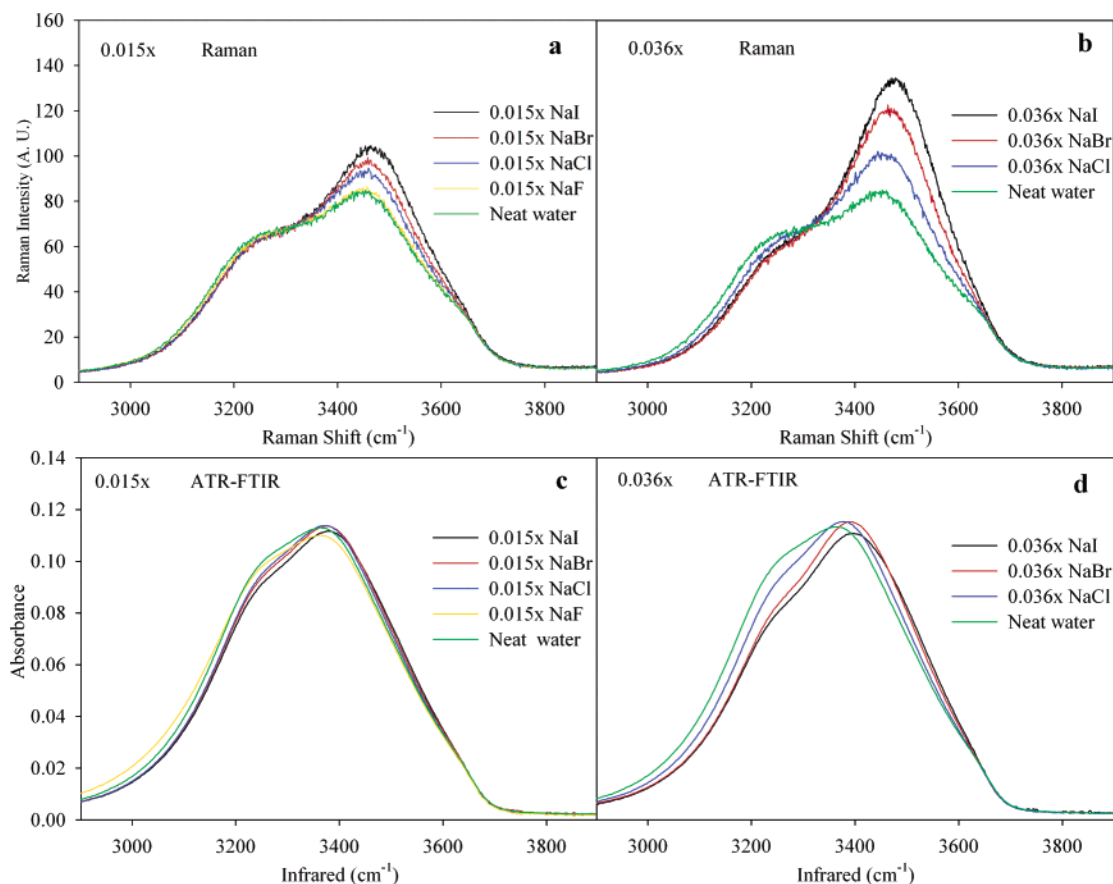


Figure 3. (a,b) Raman and (c,d) ATR-FTIR spectra of neat water and sodium halide solutions.

defined inversion center. The interface does not possess an inversion center and is therefore noncentrosymmetric and SFG active.)

The surface vibrational SFG spectra obtained from the 0.015x and 0.036x NaBr and NaI aqueous solutions are significantly different as compared to the SFG spectrum from the neat water surface as shown in Figure 4 parts c and d. The component peaks (pink dashed lines) with the calculated fits (black solid lines going through most of the data points) are shown in the insets of Figure 4 parts c and d, and the fitting parameters displayed in Table 2. For bromide and iodide anions, the larger and more polarizable halide anions, the absolute intensity of the SFG at 3700 cm^{-1} and the weakly coupled hydrogen-bonding band at 3450 cm^{-1} have slightly higher intensities than that of neat water. The intensity enhancement of these two regions (3450 and 3700 cm^{-1}) becomes stronger with increased NaBr and NaI concentration as shown in Figure 4 parts c and d. However, the calculated SFG peak fits reveal that the free OH intensity is relatively constant and the observed intensity increase is directly related to the 3450 cm^{-1} and somewhat to the 3756 cm^{-1} component peaks. The 3450 cm^{-1} region for the 0.036x NaBr and NaI solutions exhibit the largest enhancements in the SFG spectra as shown in Figure 4 parts c and d, which strongly suggests that like the bulk structure of water, the hydrogen bonding at the surface is disturbed by the addition of halide anions as the anions increase in size and polarizability. This indicates that the intermolecular coupling within the hydrogen-bonding network becomes increasingly affected. Yet, fluoride and chloride anions do not alter the intermolecular coupling of water molecules and thus the interfacial water structure. Moreover, the larger more polarizable bromide and iodide anions do perturb the interfacial water structure to a significant extent.

Water–halide hydrogen bonds are stronger than water–water hydrogen bonds, and hence the OH stretching of water halide hydrogen bonds occurs at a lower frequency than a water–water hydrogen bond. Jungwirth and Tobias¹⁶ predicted that there should be an increasing amount of red-shifted intensity in the OH stretching region for interfacial water moving in the series of F^- , Cl^- , Br^- , I^- . However, no significant red shift is observed. This is not necessarily surprising because of the difficulty in observing the solvation shell water molecules that comprise less than 5% of the interfacial water molecules for 0.015x solutions within the broad bands of the hydrogen-bonding network. The lower wavenumber region below 3000 cm^{-1} was also scanned. SFG intensity that could be identified as originating from the water–anion red-shifted vibrations was not observed.

Recall that SFG transition moments are related to Raman and IR transition moments as shown in eq 3, and the SFG intensities are modified by the number density in the interface and the orientation as shown by eqs 4 and 5. Comparison of the Raman and the IR spectra shown in Figure 3a–d to the SFG spectra shown in Figure 4a–d can therefore lead to a greater understanding of the interfacial water structure after the introduction of sodium halide salts. Similarities and differences in spectral character after deconvolution into the component peaks are observed. The ratio of the Raman peak area multiplied by the IR peak area ratio ($I_{\sim 3450}/I_{\sim 3250}$) of the components at $\sim 3450\text{ cm}^{-1}$ versus $\sim 3250\text{ cm}^{-1}$ provides additional information about the hydrogen-bonding environment.⁴⁶ Figure 5 shows the increasing trend of the $I_{\sim 3450}/I_{\sim 3250}$ ratio where solutions of neat $\text{H}_2\text{O} < \text{F}^- < \text{Cl}^- < \text{Br}^- < \text{I}^-$. These Raman \times IR intensity ratios confirm a weakening of the hydrogen bonding of the tetrahedrally coordinated water structures after adding larger and more polarizable halide anions to water; the hydrogen-bonding

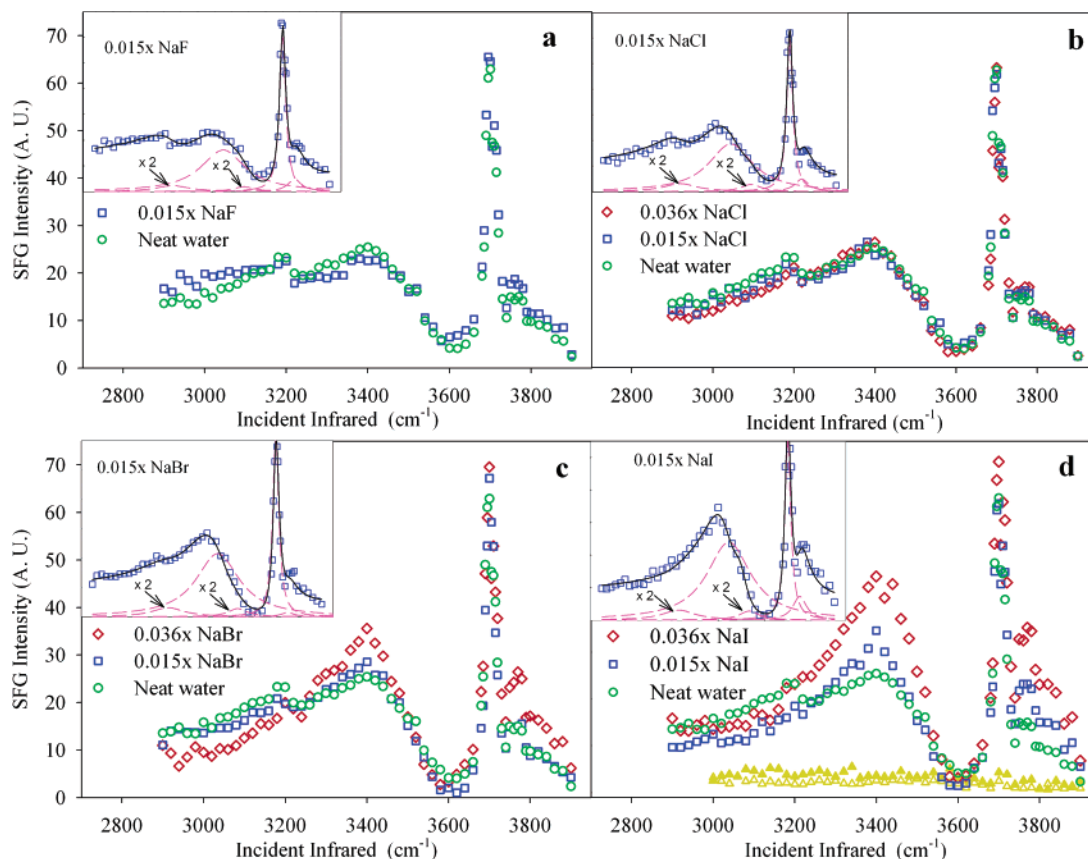


Figure 4. SSP polarized SFG spectra of (a) 0.015x NaF, (b) 0.015x and 0.036x NaCl, (c) 0.015x and 0.036x NaBr, and (d) 0.015x and 0.036x NaI. The neat water SFG spectrum is plotted in each figure for comparison. The open yellow and closed yellow triangles within (d) show the sum frequency intensity of the 0.015x NaI in D₂O and pure D₂O, respectively. Insets: SFG sodium halide aqueous solutions spectral fits. Component Lorentzian peaks are shown as dashed pink lines, and the calculated fits from the component peaks are shown as black lines that go through most of the data points.

TABLE 1: Gaussian Parameters for Raman (Figures 2b and 3a,b) and ATR-FTIR (Figures 2c and 3c,d) Spectral Fits

	Raman				ATR-FTIR			
	amplitude (A _v)	ω _v (cm ⁻¹)	FWHM	area	amplitude (A _v)	ω _v (cm ⁻¹)	FWHM	area
neat water	56.8	3256.6	250.3	15132.1	0.0718	3249.0	308.7	23.6
	68.0	3468.2	201.0	14555.7	0.0686	3420.6	267.9	19.6
	16.4	3624.0	120.8	2107.0	0.0087	3590.6	113.1	1.0
0.015x NaF	55.9	3256.6	250.3	14888.4	0.0672	3249.0	358.7	25.7
	70.1	3468.2	201.0	14992.6	0.0618	3412.3	289.8	19.1
	16.6	3624.0	120.8	2135.0	0.0065	3583.8	101.3	0.7
0.015x NaCl	54.3	3256.6	250.3	14472.5	0.0675	3249.0	301.5	21.7
	78.4	3468.2	201.0	16781.3	0.0746	3420.5	258.4	20.5
	16.4	3624.0	120.8	2115.1	0.0098	3590.7	120.1	1.3
0.036x NaCl	52.8	3256.6	250.3	14067.5	0.0636	3249.0	298.1	20.2
	87.1	3468.2	201.0	18631.2	0.0788	3420.5	256.5	21.5
	16.5	3624.0	120.8	2124.7	0.0100	3590.8	114.0	1.2
0.015x NaBr	53.4	3256.6	250.3	14211.5	0.0672	3249.0	299.2	21.4
	83.1	3468.2	201.0	17770.5	0.0757	3424.3	256.5	20.7
	16.9	3624.0	120.8	2174.6	0.0096	3592.8	113.8	1.2
0.036x NaBr	46.0	3256.6	250.3	12254.3	0.0572	3249.0	287.4	17.5
	107.0	3468.2	201.0	22889.0	0.0867	3429.1	246.8	22.8
	16.1	3624.0	120.8	2066.1	0.0097	3592.3	99.1	1.0
0.015x NaI	52.1	3256.6	250.3	13888.1	0.0667	3249.0	296.9	21.1
	89.3	3468.2	201.0	19108.5	0.0760	3428.2	253.0	20.5
	18.4	3624.0	120.8	2369.0	0.0099	3588.5	115.2	1.2
0.036x NaI	44.8	3256.6	250.3	11942.6	0.0579	3249.0	282.6	17.4
	119.2	3468.2	201.0	25492.9	0.0850	3434.8	241.3	21.8
	19.6	3624.0	120.8	2521.0	0.0109	3586.4	113.4	1.3

network is perturbed and the long range collective intermolecular couplings of symmetric stretch motions are distorted, thus, the

intensity tends to move from the 3250 cm⁻¹ region to the 3450 cm⁻¹ region. The more disordered hydrogen-bonding network

TABLE 2: Parameters for the SFG (Figures 2a and 4a–d) Spectral Fits

	amplitude (A_ν)	ω_ν (cm^{-1})	Γ_ν	area		amplitude (A_ν)	ω_ν (cm^{-1})	Γ_ν	area
neat water	+87.4	3229.6	85.9	250.6	0.015x NaBr	+30.5	3229.6	85.9	130.5
	+488.4	3446.3	115.1	5637.1		+533.7	3446.3	115.1	6729.6
	+60.7	3533.1	51.4	210.4		+17.5	3533.1	51.4	17.6
	-125.0	3700.0	16.0	2895.1		-125.7	3700.0	16.0	2944.8
	-57.8	3751.8	35.5	407.9		-42.9	3751.8	35.5	348.7
0.015x NaF	+130.3	3229.6	85.9	256.5	0.036x NaBr	+68.0	3229.6	84.9	43.8
	+462.0	3446.3	115.1	5043.1		+594.5	3435.3	112.7	10975.3
	+70.2	3533.1	51.4	281.3		-110.6	3563.1	50.9	661.3
	-126.0	3700.0	16.0	2909.9		-123.8	3700.0	16.0	2894.2
	-77.4	3751.8	35.5	414.7		-113.7	3751.8	35.5	897.5
0.015x NaCl	+77.3	3229.6	85.9	195.8	0.015x NaI	+25.1	3229.6	85.9	99.8
	+496.0	3446.3	115.1	5813.3		+563.5	3446.3	115.1	7502.1
	+51.1	3533.1	51.4	149.2		+9.3	3533.1	51.4	4.9
	-123.6	3700.0	16.0	2891.0		-124.4	3700.0	16.0	2848.5
	-78.6	3751.8	35.5	414.9		-96.0	3751.8	35.5	546.7
0.036x NaCl	+19.8	3229.6	85.9	218.6	0.036x NaI	+26.3	3229.6	84.9	26.0
	+489.8	3446.3	115.1	5727.8		+791.4	3435.3	112.7	15194.9
	+48.7	3533.1	51.4	206.9		-120.5	3563.1	50.9	851.3
	-125.0	3700.0	16.0	2875.2		-122.5	3700.0	16.0	2896.7
	-68.1	3751.8	35.5	375.9		-138.8	3751.8	35.5	1964.6

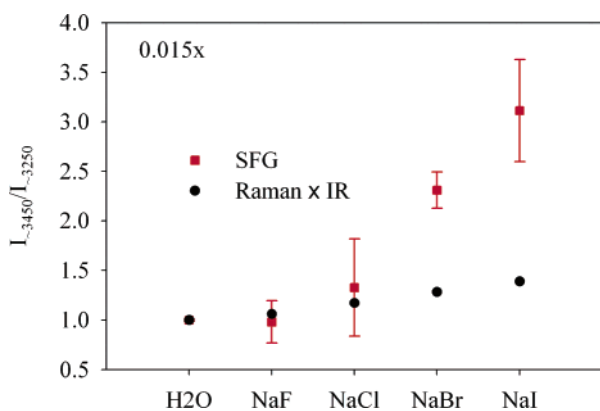


Figure 5. The ratio of the integrated peak areas of the component at $\sim 3450 \text{ cm}^{-1}$ to the component at $\sim 3250 \text{ cm}^{-1}$ for Raman multiplied by the IR and SFG spectral intensities of neat water and 0.015 mole fraction aqueous sodium halide solutions. The ratios have been normalized to neat water for the comparison between the Raman \times IR and SFG.

of the bulk prevails as one increases the size and polarizability of the halide anion that is added to the water.

Also shown in Figure 5, the SFG intensity ratios of the $\sim 3450 \text{ cm}^{-1}$ peak area to the $\sim 3250 \text{ cm}^{-1}$ peak areas ($I_{\sim 3450}/I_{\sim 3250}$) are plotted for neat water and the 0.015x sodium salts. The Raman \times IR ratio increases from H₂O and NaF to NaI. The

SFG ratios are larger than the Raman \times IR ratios for the NaBr and NaI solutions. The NaI SFG ratio is greater than the NaBr SFG ratio, which is greater than the NaCl SFG ratio ($\text{I}^- > \text{Br}^- > \text{Cl}^-$), indicating that the larger and more polarizable anions perturb the surface water structure to a greater extent. The increase from the Raman \times IR to the SFG ratio for NaBr and NaI is consistent with higher concentrations of bromide and iodide in the interfacial region as compared to the bulk concentration.

Sum frequency generation intensity (SSP polarizations) is enhanced when probing larger numbers of water molecules and/or an increased alignment of the symmetric stretch transition moment of water molecules along the surface normal. An increase in interfacial depth will increase the number of molecules probed by sum frequency spectroscopic techniques. (Recall that the interface is defined by noncentrosymmetry.) To further explore the differences in the air–liquid interfaces as affected by the different halide anions, the additive peak areas of the 3250, 3450, and 3550 cm^{-1} component peaks (these peaks were integrated from 2800 to 4000 cm^{-1} to include the distribution of the tails) are plotted in Figure 6 for the 0.015x and 0.036x sodium halide aqueous solutions. The SFG additive intensity of the tetrahedrally coordinated water molecules (including the 3550 cm^{-1} peak) increases from that of neat H₂O to that of the sodium iodide solution. This increase for the SFG

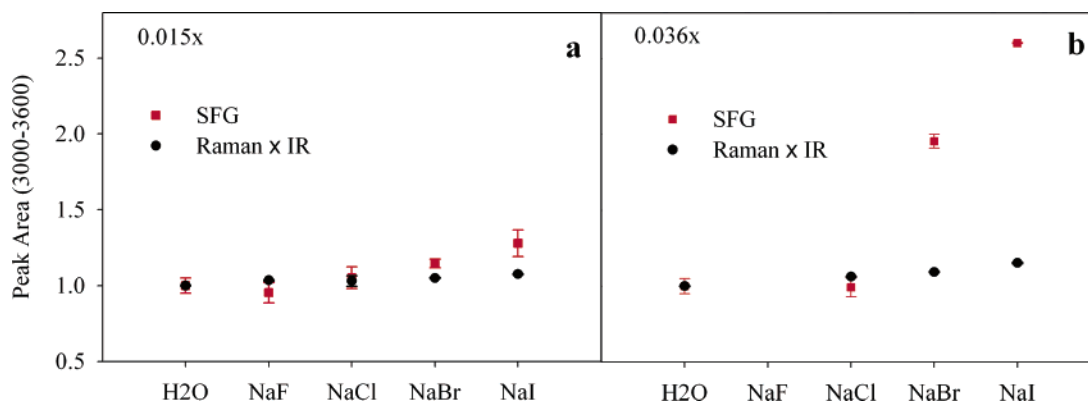


Figure 6. The areas of the 3250, 3450, and 3550 cm^{-1} (approximate, positions varied) peaks in the OH stretch region for Raman \times infrared (Raman area multiplied by ATR-FTIR area) and SFG. Areas were normalized to neat water for (a) 0.015x solutions and (b) 0.036x solutions. The interfacial depth has increased for the NaBr and NaI aqueous solutions, i.e., more water molecules are contributing to the SFG intensity of the NaBr and NaI solutions as compared to neat water, NaF, and NaCl solutions.

is significantly larger than that from the Raman \times IR results. This strongly suggests that the number of water molecules existing in the interfacial region increases with the size and polarizability of the halide added to the solution, that is, the interface becomes larger and iodide anions cause the most significant depth change. The interfacial depth is the largest for the NaI solutions, yet it is also significantly increased for the NaBr solutions. Alignment of water molecules along the surface normal is ruled out because the ions are solvated by the water (this would decrease the SFG intensity if the interfacial depth stayed constant). The interfacial depth is observed to increase from that of the air–neat water interface by increasing the concentration of the larger, more polarizable halide anions as is shown in Figure 4c,d for sodium bromide and iodide aqueous solutions. These results are consistent with the recent MD simulations^{16,17} which also reveal an increase in interfacial depth upon addition of sodium halides to water, that is, a density gradient that extends over a larger region.

Conclusions

Studies of air–aqueous sodium halide interfaces were conducted using vibrational sum frequency generation spectroscopy. Raman and IR spectroscopies were also used to compare the effects of halide anions on water structure of the bulk solution to that of the interface. The interfacial water structure for the sodium fluoride and chloride aqueous solutions are found to be similar to the air–neat water interface, whereas the interfacial water structure (the hydrogen-bonding environment) of 0.015x and 0.036x sodium bromide and iodide aqueous solutions is disturbed, that is, the hydrogen-bonding network of water molecules in the interfacial region is weakened relative to that of neat water. As the concentration of the larger and more polarizable halogen anions is increased, the interfacial region is additionally affected. Within the bulk liquid environment for the aqueous NaF, NaCl, NaBr, and NaI solutions, the water structure becomes more disordered, that is, increasing perturbation of the hydrogen-bonding network with the size and polarizability of the anion added to the water occurs. Comparison of the surface (air–liquid interface) to the bulk spectra indicates higher concentrations of Br[−] and I[−] in the interfacial region relative to the bulk. Furthermore, the interfacial depth is observed to increase after addition of NaBr and NaI to water.

Acknowledgment. We thank Professors Douglas Tobias and John Hemminger for the many discussions regarding interfacial water structure with respect to the existence of anions in the surface region of atmospheric aerosols. These original discussions motivated the studies presented here. In addition, we thank Professors Jungwirth and Tobias for sharing their manuscript¹⁶ with us prior to its publication. We acknowledge NSF for funding this project through the NSF Ohio State Environmental Molecular Science Institute (CHE-0089147), as well as Research Corporation for partial support of this research.

References and Notes

- (1) Tarasick, D. W.; Bottenheim, J. W.; Gallant, A. G.; Brice, K. A. *Atmos. Chem. Phys.* **2002**, *2*, 197–205.
- (2) Bottenheim, J. W.; Gallant, A. G.; Brice, K. A. *Geophys. Res. Lett.* **1986**, *13*, 113–116.
- (3) Anlauf, K. G.; Mickle, R. E.; Trivett, N. B. A. *J. Geophys. Res.* **1994**, *25*, 345–353.
- (4) Foster, K. L.; Tolbert, M. A.; George, S. M. *J. Phys. Chem. A* **1997**, *101*, 4979–4986.
- (5) Knipping, E. M.; Lakin, M. J.; Foster, K. L.; Jungwirth, P.; Tobias, D. J.; Gerber, R. B.; Dabdub, D.; Finlayson-Pitts, B. J. *Science* **2000**, *288*, 301–306.
- (6) Oum, K. W.; Lakin, M. J.; DeHaan, D. O.; Brauers, T.; Finlayson-Pitts, B. J. *Science* **1998**, *279*, 74.
- (7) Foster, K. L.; Plastringe, R. A.; Bottenheim, J. W.; Gallant, A. G.; Brice, K. A.; Shepson, P. B.; Finlayson-Pitts, B. J. *Science* **2001**, *291*, 471–474.
- (8) Cho, H.; Shepson, P. B.; Barrie, L. A.; Cowin, J. P.; Zaveri, R. J. *Phys. Chem. B* **2002**, *106*, 11226–11232.
- (9) Martin, S.; Yu, Y.; Drucker, R. J. *Geophys. Res.* **1996**, *101*, 12111.
- (10) Perovich, D. K.; Richer-Menge, J. A. *J. Geophys. Res.* **1994**, *99*, 16341.
- (11) Richter, A.; Wittrock, F.; Eisinger, M.; Burrows, J. P. *Geophys. Res. Lett.* **1998**, *25*, 2863–2886.
- (12) McElroy, C. T.; McLinden, C. A.; McConnell, J. C. *Nature* **1999**, *397*, 338–340.
- (13) Hu, J. H.; Shi, Q.; Davidovits, P.; Worsnop, D. R.; Zahniser, M. S.; Kolb, C. E. *J. Phys. Chem.* **1995**, *99*, 8768–76.
- (14) Adam, N. K. *The Physics and Chemistry of Surfaces*; Oxford University Press: London, 1941.
- (15) Chattoraj, D. K.; Birdi, K. S. *Adsorption and the Gibbs Surface Excess*; Plenum: New York, 1984.
- (16) Jungwirth, P.; Tobias, D. J. *J. Phys. Chem. B* **2001**, *105*, 10468–10472.
- (17) Jungwirth, P.; Tobias, D. J. *J. Phys. Chem. B* **2002**, *106*, 6361–6373.
- (18) Shen, Y. R. *The Principles of Nonlinear Optics*, 1st ed.; John Wiley & Sons: New York, 1984.
- (19) Bloembergen, N.; Pershan, P. S. *Phys. Rev.* **1962**, *128*, 606–621.
- (20) Miranda, P. B.; Shen, Y. R. *J. Phys. Chem. B* **1999**, *103*, 3292–3307.
- (21) Hirose, C.; Akamatsu, N.; Domen, K. *Appl. Spectrosc.* **1992**, *46*, 1051–1072.
- (22) Morita, A.; Hynes, J. T. *Chem. Phys.* **2000**, *258*, 371–390.
- (23) Hommel, E. L.; Allen, H. C. *Anal. Sci.* **2001**, *17*, 137–139.
- (24) Hommel, E. L.; Ma, G.; Allen, H. C. *Anal. Sci.* **2001**, *17*, 1325–1329.
- (25) Ma, G.; Allen, H. C. *J. Am. Chem. Soc.* **2002**, *124*, 9374–9375.
- (26) Hommel, E. L.; Allen, H. C. *Analyst* **2003**, *128*, 750–755.
- (27) Ma, G.; Allen, H. C. *J. Phys. Chem. B* **2003**, *107*, 6343–6349.
- (28) Hommel, E. L.; Allen, H. C. *J. Phys. Chem. B* **2003**, *107*, 10823–10828.
- (29) Allen, H. C.; Raymond, E. A.; Richmond, G. L. *J. Phys. Chem. A* **2001**, *105*, 1649–1655.
- (30) Shultz, M. J.; Baldelli, S.; Schnitzer, C.; Simonelli, D. *J. Phys. Chem. B* **2002**, *106*, 5313–5324.
- (31) Du, Q.; Superfine, R.; Freysz, E.; Shen, Y. R. *Phys. Rev. Lett.* **1993**, *70*, 2313–2316.
- (32) Schnitzer, C.; Baldelli, S.; Campbell, D. J.; Shultz, M. J. *J. Phys. Chem. A* **1999**, *103*, 6383–6386.
- (33) Allen, H. C.; Raymond, E. A.; Richmond, G. L. *Curr. Opin. Colloid Interface Sci.* **2000**, *5*, 74–80.
- (34) Lilley, T. H. Raman Spectroscopy of Aqueous Electrolyte Solutions. In *Water, A Comprehensive Treatise*; Frank, F., Ed.; Plenum Press: New York, 1973; Vol. 3.
- (35) Verrall, R. E. Infrared Spectroscopy of Aqueous Electrolyte Solutions. In *Water, A Comprehensive Treatise*; Frank, F., Ed.; Plenum Press: New York, 1973; Vol. 3.
- (36) Walrafen, G. E.; Chu, Y. C. *J. Phys. Chem.* **1995**, *99*, 11225–11229.
- (37) Walrafen, G. E.; Yang, W.-H.; Chu, Y. C. Raman Evidence for the Clathratelike Structure of Highly Supercooled Water. In *Supercooled Liquids*; American Chemical Society: Washington, DC, 1997; Chapter 21, pp 287–308.
- (38) Shen, Y. R. *Solid State Commun.* **1998**, *108*, 399–406.
- (39) Buck, U.; Ettischer, I.; Melzer, M.; Buch, V.; Sadlej, J. *Phys. Rev. Lett.* **1998**, *80*, 2578–2581.
- (40) Devlin, J. P.; Sadlej, J.; Buch, V. *J. Phys. Chem. A* **2001**, *105*, 974–983.
- (41) Pribble, R. N.; Zwier, T. S. *Science* **1994**, *265*, 75–79.
- (42) Robinson, G. W.; Zhu, S.-B.; Singh, S.; Evans, M. W. *Water in Biology, Chemistry and Physics—Experimental Overviews and Computational Methodologies*; World Scientific: River Edge, NJ, 1996; Vol. 9.
- (43) Devlin, J. P.; Buch, V. *J. Phys. Chem.* **1995**, *99*, 16534–16548.
- (44) Buch, V.; Devlin, J. P. *J. Chem. Phys.* **1999**, *110*, 3437–3443.
- (45) Green, J. L.; Lacey, A. R.; Sceats, M. G. *J. Phys. Chem.* **1986**, *90*, 3958–64.
- (46) Marinov, V. S.; Nikolov, Z. S.; Matsuura, H. *J. Phys. Chem. B* **2001**, *105*, 9953–9959.
- (47) Micali, N.; Vasi, C.; Mollamace, F.; Corti, M.; Degiorgio, V. *Phys. Rev. E* **1993**, *48*, 3661–6.
- (48) Raymond, R. A.; Tarback, T. L.; Brown, M. G.; Richmond, G. L. *J. Phys. Chem. B* **2003**, *107*, 546–556.

(49) Scherer, J. R. The Vibrational Spectroscopy of Water. In *Advances in Infrared and Raman Spectroscopy*; Clark, R. J. H., Hester, R. E., Eds.; Heyden: Philadelphia, 1978; Vol. 5, Chapter 3, pp 149–216.

(50) Raymond, E., A.; Tarbuck, T. L.; Richmond, G. L. *J. Phys. Chem. B* **2002**, *106*, 2871–2820.

(51) Gruenloh, C. J.; Carney, J. R.; Hagemeister, F. C.; Arrington, C. A.; Zwier, T. S.; Fredericks, S. Y.; Wood, J. T. I.; Jordan, K. D. *J. Chem. Phys.* **1998**, *109*, 6601–6614.

(52) Rowland, B.; Fisher, M.; Devlin, J. P. *J. Chem. Phys.* **1991**, *95*, 1378–1384.

(53) Terpstra, P.; Combes, D.; Zwick, A. *J. Chem. Phys.* **1990**, *92*, 65–70.

(54) Jungwirth, P.; Tobias, D. J. *J. Phys. Chem. A* **2002**, *106*, 379–383.

(55) Schnitzer, C.; Baldelli, S.; Shultz, M. J. *J. Phys. Chem. B* **2000**, *104*, 585–590.